ACS NANO

www.acsnano.org

Field-Induced Rotational Symmetry Distortion of In-Plane Anisotropic Magnetoresistance in Kagome Semimetal $Ni_3In_2Se_2$ Nanoflakes

Senhao Lv,[⊥] Hui Guo,[⊥] Yuhui Li, Guojing Hu, Guolin Wan, Ruwen Wang, Guoyu Xian, Xinwei Yi, Zhen Zhao, Nan Si, Ke Zhu, Yechao Han, Lihong Bao, Xiao Lin, Shixuan Du, Jinbo Pan,* Jun He,* Haitao Yang,* and Hong-Jun Gao

Cite This: *ACS Nano* 2026, 20, 21316−21326

Read Online

ACCESS | Metrics & More | Article Recommendations | Supporting Information

ABSTRACT: **Transition-metal-based kagome compounds have recently attracted considerable attention due to their rich correlated electronic states and unconventional quantum transport phenomena, as well as their potential for anisotropic magnetotransport functionalities. Here, we report magnetic field-induced rotational symmetry distortion of the in-plane anisotropic magnetoresistance (AMR) in kagome semimetal $Ni_3In_2Se_2$ nanoflakes synthesized via an iterative chemical vapor transport approach. High-quality $Ni_3In_2Se_2$ nanoflakes possess a canted ferromagnetic order, along with a large magnetoresistance of 590%, an out-of-plane AMR of 200%, and a carrier mobility up to 8761 $cm^2 V^{-1} s^{-1}$. Furthermore, a large in-plane AMR of 41% and the planar Hall effect (PHE) are detected in $Ni_3In_2Se_2$, with PHE stemming from the complex interaction of field-induced ferromagnetism and orbital magnetoresistance. Notably, the in-plane AMR exhibits a field-induced rotational symmetry distortion, characterized by the coexistence of the two-, four-, and six-fold AMR components. Band structure calculations suggest that the low-temperature distortions in the AMR of $Ni_3In_2Se_2$ may arise from field-induced orbital polarization and field-enhanced Fermi surface anisotropy. Our findings contribute to understanding exotic transport behaviors in kagome semimetals and advancing low-power electronic devices and future spintronic applications.**

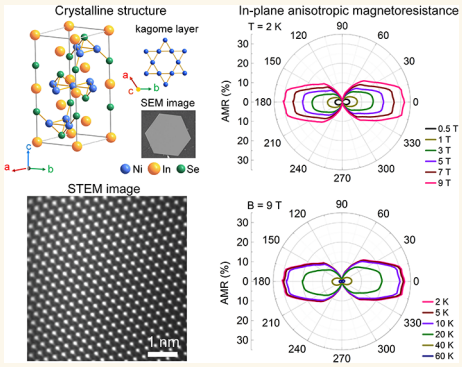

KEYWORDS: *$Ni_3In_2Se_2$ nanoflakes, kagome semimetal, anisotropic magnetoresistance, planar Hall effect, rotational symmetry distortion*

Kagome-lattice materials, composed of a two-dimensional network of corner-sharing triangles, have attracted significant interest owing to their interplay between lattice geometry, electron correlation, and nontrivial band topology.[1−3] The distinctive kagome lattice gives rise to geometric frustration and supports characteristic electronic features such as flat bands, Dirac dispersions, and van Hove singularities. When combined with strong electron correlations and spin−orbit coupling, it offers a fertile ground for a variety of emergent quantum phases, including quantum Hall states, quantum spin liquids, magnetic topological phases, etc.[4−8] In particular, magnetic kagome semimetals constitute a distinctive subclass, exhibiting Berry-curvature-driven anomalous Hall effect, spin−orbit polarons, chiral anomaly, and pronounced anomalous Nernst response.[9−14] Representative systems such as antiferromagnetic Mn_3Sn and ferromagnetic $Co_3Sn_2S_2$ have demonstrated large anomalous Hall conductivity and topology-related transport signatures arising from Weyl Fermions and nontrivial Berry curvature.[14,15] In addition, complex spin textures in kagome magnets can generate emergent real-space Berry curvature, leading to topological Hall and topological Nernst effects in systems such as FeGe[16] and $ErMn_6Sn_6$,[17] further highlighting the rich interplay between topology, magnetism, and electronic transport in kagome systems. These exceptional properties establish kagome semimetals as fertile ground for exploring exotic magnetotransport phenomena, thereby advancing high-performance electronics and spintronics applications.

Recently, anisotropic magnetoresistance (AMR) and the planar Hall effect (PHE) have emerged as key manifestations of spin-dependent transport in kagome semimetals, holding

Received: April 9, 2026
Revised: July 15, 2026
Accepted: July 15, 2026
Published: July 20, 2026

ACS Publications © 2026 American Chemical Society

https://doi.org/10.1021/acsnano.6c06737
ACS Nano 2026, 20, 21316−21326

Downloaded from pubs.acs.org/ancac3/article-pdf/20/30/21316/66049429/acsnano.6c06737.pdf by INST OF PHYSICS user on 30 September 2026

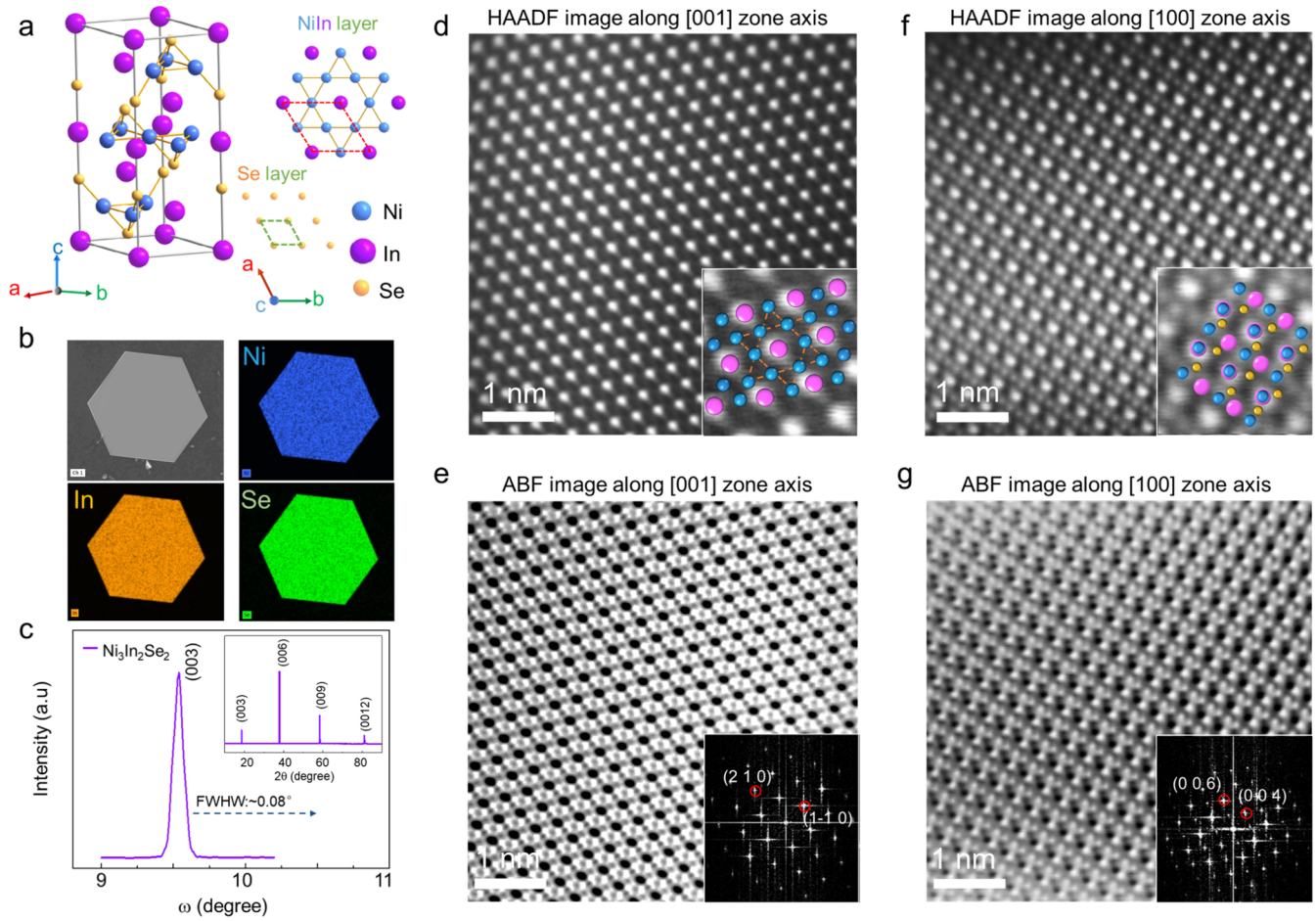

Figure 1. Crystal structure characterization of hexagonal single-crystalline $Ni_3In_2Se_2$ flakes. (a) Crystal structure of $Ni_3In_2Se_2$. The Ni atoms form a two-dimensional kagome lattice. Blue, pink, and yellow balls represent Ni, In, and Se atoms, respectively. (b) Color maps of Ni, In, and Se elements, showing uniform distributions of these three elements within the hexagonal-shaped sample. (c) X-ray rocking curves of (003) reflection for the single-crystalline $Ni_3In_2Se_2$ flake by the iterative-CVT method, showing a notably small fwhm of ∼0.08°. The inset shows the X-ray diffraction pattern of the single-crystalline $Ni_3In_2Se_2$ flake. (d, e) High-resolution HAADF and ABF images of the single-crystalline $Ni_3In_2Se_2$ flake structure seen along the [001] zone axis, up and down, respectively. (f, g) High-resolution HAADF and ABF images of the single-crystalline $Ni_3In_2Se_2$ flake structure seen along the [100] zone axis, up and down, respectively.

potential for high-sensitivity magnetic sensors and low-power electronic devices.[18,19] The PHE emerges under in-plane magnetic fields and generates an angle-dependent transverse voltage,[20−22] whereas AMR, which describes the variation of electrical resistance with the angle between current and magnetization, has been extensively utilized to reveal Fermi surface symmetry, detect hidden electronic phases, and explore potential topological phase transitions.[23,24] Generally, the angular dependence of magnetoresistance in magnetic systems originates from relativistic spin−orbit coupling, which modifies the electronic states near the Fermi level under an applied magnetic field,[25,26] with the AMR symmetry reflecting the crystal and magnetic sublattice symmetries and typically exhibiting a 2-fold angular dependence. Unlike common 2-fold AMR, anomalous AMR exhibits higher-order angular patterns and symmetry breaking that typically emerge in conjunction with phase transitions, such as metamagnetic transitions, topological phase changes, or variations in carrier density, and has drawn increasing interest due to its potential for applications in spintronic devices and low-power electronics.[27−30] Given the coexistence of frustrated magnetism and nontrivial electronic structures in kagome materials, anomalous AMR responses are anticipated, yet remain largely unexplored.

In this work, we report magnetotransport properties of kagome semimetal $Ni_3In_2Se_2$ nanoflakes synthesized via an iterative chemical vapor transport (iterative-CVT) method. Magnetic measurements reveal a canted ferromagnetic ground state, accompanied by a field-induced out-of-plane ferromagnetic component. Low-temperature transport measurements reveal large magnetoresistance up to 590% (7 T) and high carrier mobility of 8761 $cm^2 V^{-1} s^{-1}$. Remarkably, pronounced in-plane AMR (41%) and PHE are observed, with the AMR exhibiting magnetic-field-induced rotational symmetry distortion characterized by the coexistence of 2-fold, 4-fold, and 6-fold components. On the basis of first-principles calculations, the observed rotational symmetry distortions may arise from field-induced orbital polarization and field-enhanced Fermi surface anisotropy. Our work offers insights into exotic transport responses and contributes to the development of low-dissipation electronic and spintronic devices.

https://doi.org/10.1021/acsnano.6c06737
ACS Nano 2026, 20, 21316−21326

Downloaded from pubs.acs.org/ancac3/article-pdf/20/30/21316/66049429/acsnano.6c06737.pdf by INST OF PHYSICS user on 30 September 2026

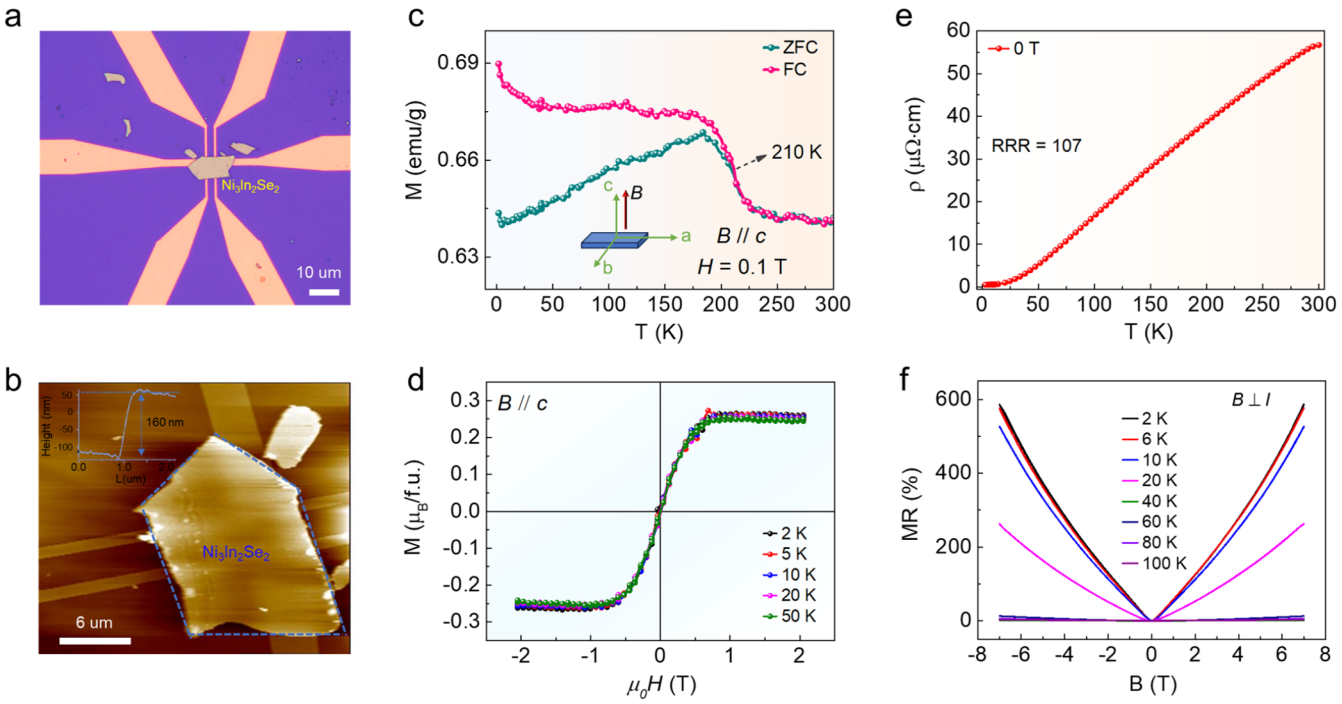

Figure 2. Magnetic Properties, resistivity, and magnetoresistance of $Ni_3In_2Se_2$ nanoflakes. (a) Optical microscope image of the $Ni_3In_2Se_2$ nanoflake device. (b) Atomic force microscope imaging of the $Ni_3In_2Se_2$ nanoflake with a thickness of 160 nm. (c) Temperature dependence of magnetization with ZFC and FC procedures of $Ni_3In_2Se_2$ nanoflakes under 0.1 T with the field applied along the *c*-axis. (d) Field dependence of the out-of-plane magnetization for $B//c$ at various temperatures ranging from 2 to 50 K. (e) Temperature dependence of the resistivity under 0 T. (f) Magnetoresistance measured under applied fields up to 7 T at different temperatures from 2 to 100 K for $B\perp I$.

RESULTS AND DISCUSSION

The $Ni_3In_2Se_2$ flakes crystallize in a rhombohedral structure of the space group, $R\bar{3}m$ (No. 166), in which Ni atoms form a two-dimensional kagome lattice sandwiched between two Se atomic planes located above and below the Ni kagome layer, while In atoms occupy the centers of the hexagonal motifs. (Figure 1a). High-quality single-crystalline $Ni_3In_2Se_2$ hexagonal flakes are synthesized by the iterative-CVT method, with small single-crystal granules of $Ni_3In_2Se_2$ taken as the vapor source and halide as the transport agent (Figure S1a). The synthesized single-crystalline $Ni_3In_2Se_2$ flakes show a regular hexagonal shape, suggesting the preferred growth of the *ab*-plane. The component of single-crystalline $Ni_3In_2Se_2$ flakes was detected by the X-ray energy-dispersive spectroscopy (EDS), with the stoichiometric ratio of Ni:In:Se very close to 3:2:2 (Figure S1b), and elemental color maps of Ni, In, and Se reveal the uniform distributions of all three elements across the hexagonal-shaped sample (Figure 1b). The X-ray rocking curve of the (003) Bragg reflection exhibits a markedly smaller full width at half-maximum (fwhm) of 0.08° for the iterative-CVT-grown $Ni_3In_2Se_2$ flakes (Figure 1c), compared with 0.125° for the self-flux-grown crystals (Figure S1c), demonstrating the enhanced crystalline quality of the iterative-CVT-grown $Ni_3In_2Se_2$ flakes. The inset of Figure 1c shows the X-ray diffraction (XRD) pattern, only exhibiting the (*00l*) diffraction peaks. The crystallographic data and structure refinement results for the single-crystalline $Ni_3In_2Se_2$ flakes are presented in Figure S2, with refined lattice parameters of $a = b = 5.418$ Å and $c = 14.213$ Å. Moreover, the (*h0l*) plane diffraction pattern of $Ni_3In_2Se_2$ exhibits sharp and well-defined diffraction spots without splitting (Figure S3).

The high-resolution transmission electron microscopy (HRTEM) measurement on the single-crystalline $Ni_3In_2Se_2$ flake shows a lattice spacing of 0.271 nm, corresponding to the (−120) plane of $Ni_3In_2Se_2$ (Figure S3), which is consistent with the selected area electron diffraction (SAED) pattern shown in the inset. To further assess the quality of the synthesized single-crystalline $Ni_3In_2Se_2$ flakes, atomic-scale analysis was performed on cross-sectional samples using aberration-corrected scanning transmission electron microscopy (STEM). Figure 1d,e shows the simultaneously acquired STEM high-angle annular dark-field (HAADF) image and annular bright-field (ABF) images of $Ni_3In_2Se_2$ along the [001] axis, with the overlaid structural model and an indexed Ni_3In kagome plane, clearly revealing a clean *ab*-plane with a well-defined hexagonal lattice structure. Moreover, the simultaneously acquired HAADF image and ABF images of $Ni_3In_2Se_2$ along the [100] axis reveal the perfect crystalline structure of the single-crystalline $Ni_3In_2Se_2$ flakes without noticeable defects (Figures 1f,g and S4). These results confirm the single-phase purity and high crystallinity of the as-grown single-crystal $Ni_3In_2Se_2$ flakes.

Figure S5 illustrates the schematic process of lifting $Ni_3In_2Se_2$ nanoflakes from the inner wall of a quartz tube and transferring them onto a SiO_2/Si substrate with prepatterned electrodes using a PPC film. The nanoflakes are initially picked up by the PPC film from the quartz plate and then transferred onto the electrode substrate at 95 °C. Residual PPC is subsequently removed using an acetone solution. An optical microscope image of the fabricated device is shown in Figure 2a, and the corresponding atomic force microscopy (AFM) image in Figure 2b reveals a $Ni_3In_2Se_2$ nanoflake with a thickness of approximately 160 nm. As shown in Figures 2c and S6a, the temperature-dependent magnetization of the

https://doi.org/10.1021/acsnano.6c06737
ACS Nano 2026, 20, 21316−21326

Downloaded from pubs.acs.org/ancac3/article-pdf/20/30/21316/66049429/acsnano.6c06737.pdf by INST OF PHYSICS user on 30 September 2026

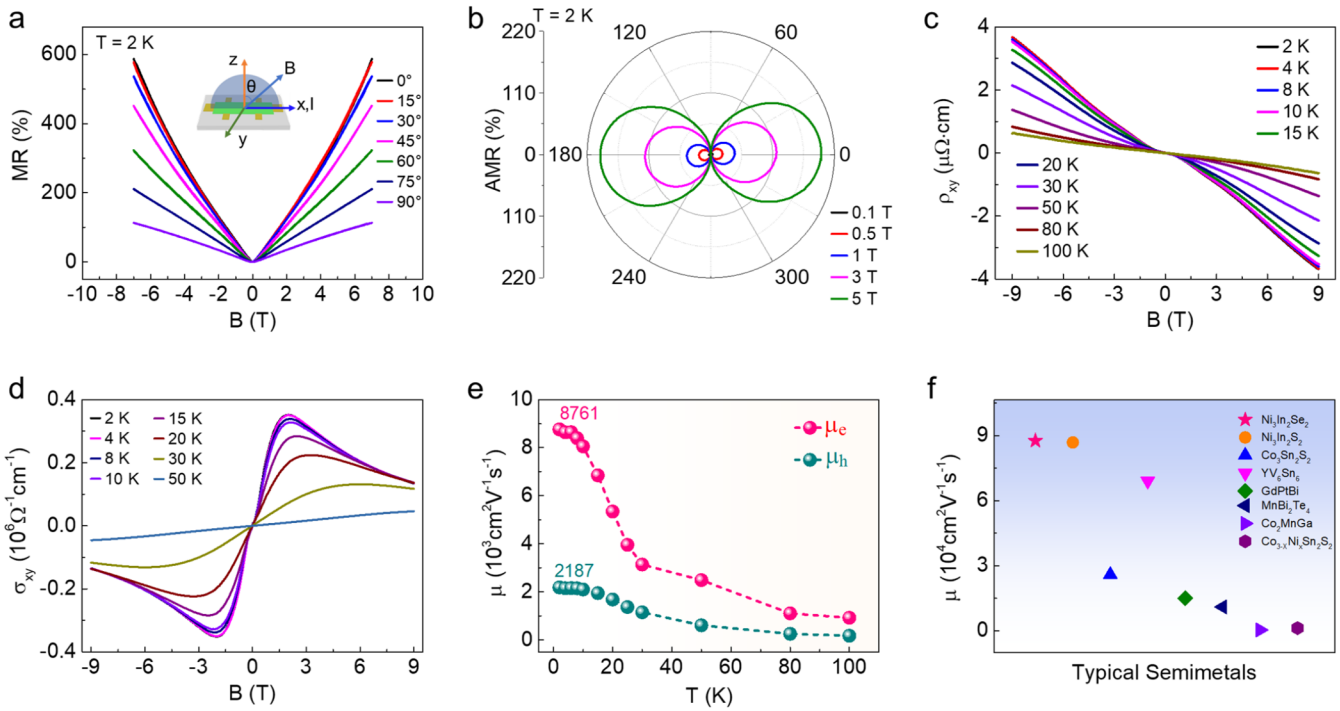

Figure 3. Out-of-plane AMR, Hall resistivity, and carrier mobility of the $Ni_3In_2Se_2$ nanoflake. (a) Magnetic field dependence of magnetoresistance at 2 K with different field-orientation angles θ_{zx}. The inset shows the schematic of the measurement configuration. (b) Angle dependence of magnetoresistance at different fields from 0.1 to 5 T at 2 K. (c) Field-dependent ρ_{xy} measured at different temperatures from 2 to 100 K in an out-of-plane configuration with $B \perp I$. (d) Field-dependent the Hall conductivity σ_{xy} at different temperatures from 2 to 50 K. (e) Temperature dependence of carrier mobilities (μ_e and μ_h), showing the maximum mobility of 8761 and 2187 $cm^2\ V^{-1}\ s^{-1}$ for electron and hole at 2 K, respectively. (f) Comparison of carrier mobilities of topological semimetal materials.

$Ni_3In_2Se_2$ nanoflakes, measured under magnetic fields of 0.05 and 0.1 T along the *c*-axis, reveals a ferromagnetic-like transition near 210 K, as well as a pronounced upturn below 10 K, suggesting the presence of an additional low-temperature magnetic transition. Compared with the magnetization curves measured under 0.05 and 0.1 T, the low-temperature upturn observed under 0.5 T is significantly more noticeable (Figure S6b), indicating that the spin configuration at low temperatures exhibits a strong field dependence. Such behavior suggests that the magnetic moments are not fully aligned in the low-field regime, and that a higher field may promote a transition toward a more collinear or ferromagnetic-like state, possibly through a spin reorientation or a field-induced metamagnetic crossover.

Figure 2d displays the field dependence of magnetization with the field along the *c*-axis at different temperatures from 2 to 50 K, showing an out-of-plane ferromagnetic order with a saturation magnetization (M_s) of 0.085 μ_B per Ni atom. The magnetization curves exhibit only a weak temperature dependence between 2 and 50 K, which may be attributed to the strong magnetic interactions and pronounced magnetic anisotropy of $Ni_3In_2Se_2$ that help maintain a robust spin configuration and magnetic order against thermal perturbations. Although the thermal energy increases with temperature, it remains insufficient to significantly perturb the magnetically ordered state or induce substantial spin reorientation within this temperature range, resulting in only a slight reduction in magnetization. The temperature dependence of magnetization of the $Ni_3Sn_2Se_2$ nanoflakes under a magnetic field of 0.1 T applied along the *ab*-plane (Figure S6c) shows a much lower magnetization compared to that along the *c*-axis, indicating a weak magnetic response in the *ab*-plane. Figure S6d shows that the in-plane magnetization of $Ni_3Sn_2Se_2$ remains nearly linear and unsaturated up to 2 T, and reaches only about one-third of the out-of-plane value at 2 K, indicating the strong magnetic anisotropy with the *c*-axis as the easy magnetization direction. Calculations further support this scenario, revealing a canted ferromagnetic ground state consistent with the noncollinear arrangement inferred from the magnetization data (Figure S7a). Based on the magnetization behavior, a possible evolution of the magnetic structure in $Ni_3Sn_2Se_2$ is proposed, as illustrated in the lower panel of Figure S7b. Above 210 K, the system remains paramagnetic with disordered spins. Upon cooling below 210 K, a magnetically ordered state develops, likely characterized by a canted spin configuration such as a conical helical order,[31,32] giving rise to a finite out-of-plane net moment. A further upturn in magnetization below ∼10 K suggests a spin reorientation or an increased net magnetization.

The temperature dependence of the longitudinal electrical resistivity (ρ_{xx}) of $Ni_3In_2Se_2$ under the zero magnetic field along the *z* direction (*c*-axis) is shown in Figures 2e and S8a, revealing a smaller residual resistivity of 0.5304 $\mu\Omega$·cm and a larger residual resistivity ratio (RRR = ρ_{300K}/ρ_{2K}) of 107 for the iterative-CVT-grown single-crystalline $Ni_3In_2Se_2$ nanoflakes, whereas the $Ni_3In_2Se_2$ bulk single crystal exhibits a higher residual resistivity of 1.61 $\mu\Omega$·cm and a smaller RRR of 20. At low temperatures, the residual resistivity is primarily governed by temperature-independent scattering sources, while the phonon scattering is largely suppressed. Structural imperfections can act as carrier-scattering centers, shortening the carrier mean free path and thereby increasing the residual resistivity. Therefore, the significantly lower residual resistivity

https://doi.org/10.1021/acsnano.6c06737
ACS Nano 2026, 20, 21316−21326

Downloaded from pubs.acs.org/ancac3/article-pdf/20/30/21316/66049429/acsnano.6c06737.pdf by INST OF PHYSICS user on 30 September 2026

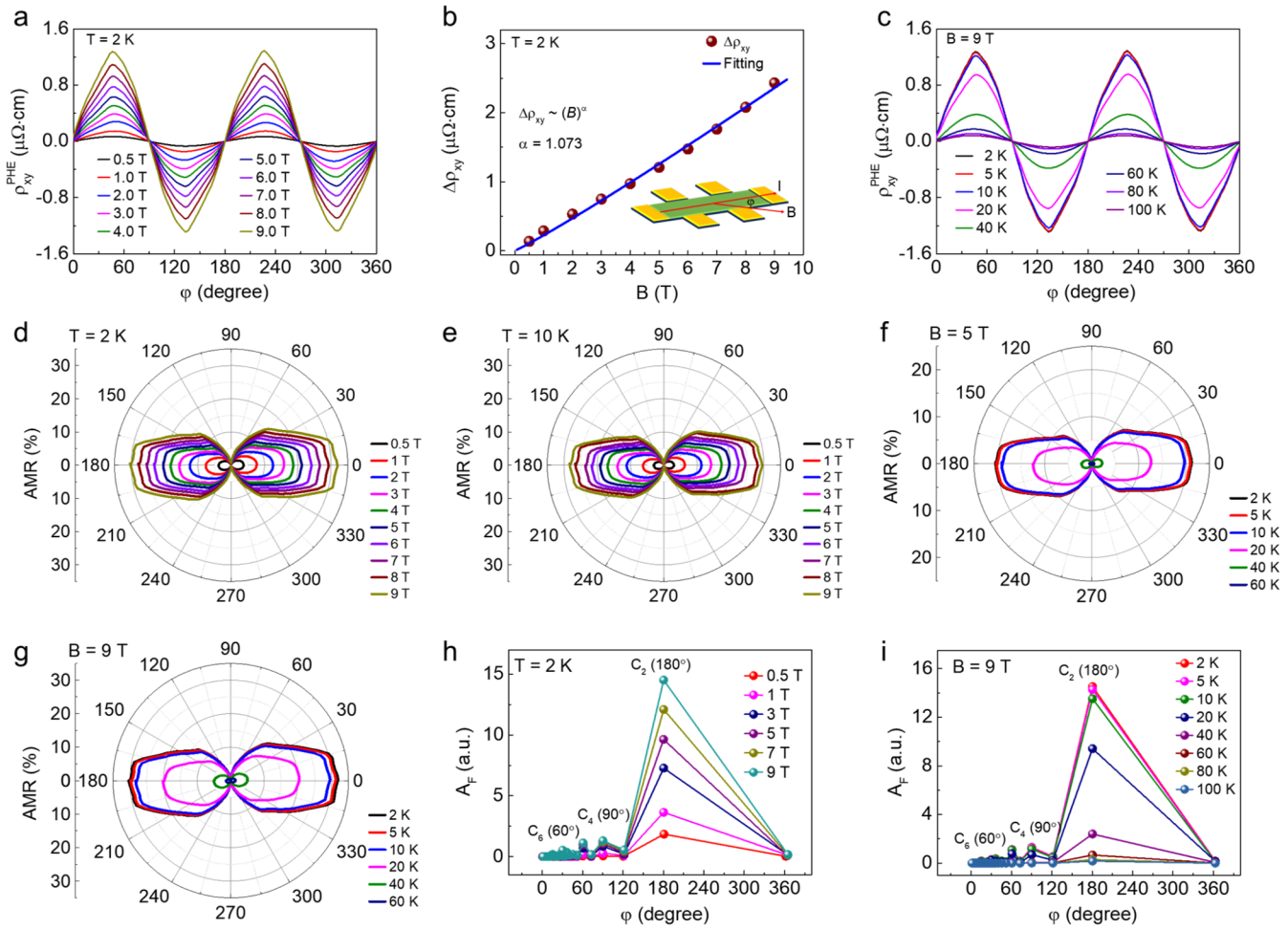

Figure 4. In-plane anomalous anisotropic magnetoresistance and planar Hall effect of the $Ni_3In_2Se_2$ nanoflake. (a) Planar Hall resistivity at 2 K under different magnetic fields from 0.5 to 9 T. (b) Field dependence of $\Delta\rho_{xy}$ obtained from fitting, following a power law with an exponent of 1.073. The lower inset illustrates a typical PHE measurement setup, where both longitudinal and transverse voltages, corresponding to in-plane AMR and planar Hall resistivity, are measured as the magnetic field *B* rotates in the *ab*-plane. (c) Planar Hall resistivity under 9 T at different temperatures from 2 to 100 K. (d, e) Angle dependence of magnetoresistance at 2 and 10 K under different fields from 0.5 to 9 T. (f, g) Angle dependence of magnetoresistance under 5 and 9 T at temperatures ranging from 2 to 60 K. (h) FT results to the in-plane AMR cures measured at 2 K under different fields from 0.5 to 9 T, exhibiting a superposition of the 2-fold, 4-fold and 6-fold AMR terms. (i) FT results to the in-plane AMR curves measured under 9 T from 2 to 100 K.

and larger RRR observed in the iterative-CVT-grown $Ni_3In_2Se_2$ nanoflakes indicate the reduced defect-induced carrier scattering and enhanced crystalline quality. In addition, the resistivity of the $Ni_3In_2Se_2$ nanoflake in the low temperature ranging from 2 to 100 K can be well described by a relation: $\rho(T) = \rho_{xx}(0) + bT^m$, as shown in the inset of Figure S8b, where $\rho_{xx}(0)$ is the residual resistivity and b is a constant factor. The fitting results yield an exponent of $m \sim 1.82$, indicating that electron−electron interactions dominate in $Ni_3In_2Se_2$ at low temperatures from 2 to 100 K. Figure 2f reveals the magnetic-field-dependent magnetoresistance ($MR = [\rho_{xx}(\mu_0 H) - \rho_{xx}(0)]/\rho_{xx}(0)\times100\%$) for the $Ni_3In_2Se_2$ nanoflake under the out-of-plane fields at different temperatures from 2 to 100 K, exhibiting a nonsaturated positive MR of up to 590% under 7 T at 2 K. To better understand the variation of *MR*, we conduct a power law fitting at temperatures of 2, 6, 10, and 20 K by the Kohler rule: $MR = a\cdot(m_0H/\rho_0)^n$, where ρ_0 is the zero-field resistivity at a specific temperature and a and m are the constants (Figure S8c). The fitting results give an exponent of $n \sim 1.3$, suggesting semimetallic characteristics for $Ni_3In_2Se_2$ nanoflakes.[33,34]

To further explore the impact of magnetic field orientation on resistivity, we studied the *MR* in the angle range from 0° to 90° with the magnetic field rotating along the *z*-*x*-plane, manifesting that the positive magnetic resistance gradually decreases as the angle increases (Figure 3a). The angular dependence of the out-of-plane AMR at 2 K (Figure 3b) shows a 2-fold symmetry under different magnetic fields, with an anisotropy value of 200% at 5 T, indicating extremely strong out-of-plane anisotropy in the $Ni_3In_2Se_2$ nanoflake. The observed notable magnetoresistance effects in $Ni_3In_2Se_2$ could endow a vast potential for the advancement of high-performance electronic and spintronic devices. We further investigated the out-of-plane Hall effect of the $Ni_3In_2Se_2$ nanoflake. Figure 3c shows the field-dependent ρ_{xy} at different temperatures from 2 to 100 K, in an out-of-plane configuration with $B\perp I$, which displays a nonlinear behavior that persists up to 100 K, indicating the typical characteristic of multitype carriers.

To further characterize the conductivity of the $Ni_3In_2Se_2$ nanoflake, Hall conductivity (σ_{xy}) and longitudinal conductivity (σ_{xx}) as the important characteristic parameters are given by

https://doi.org/10.1021/acsnano.6c06737
ACS Nano 2026, 20, 21316−21326

Downloaded from pubs.acs.org/ancac3/article-pdf/20/30/21316/66049429/acsnano.6c06737.pdf by INST OF PHYSICS user on 30 September 2026

$\sigma_{xy} = \frac{-\rho_{xy}}{\rho_{xy}^2 + \rho_{xx}^2}$ and $\sigma_{xx} = \frac{\rho_{xx}}{\rho_{xy}^2 + \rho_{xx}^2}$, respectively, in which ρ_{xx} is the longitudinal resistivity. The field-dependent σ_{xy} from 2 and 50 K exhibits significant nonlinear behavior as the temperature decreases, indicating the enhancement of the two-carrier conduction effect, with a maximum Hall conductivity of 3.5 × 10^5 $\Omega^{-1}cm^{-1}$ under a field of 2 T (Figure 3d). The temperature dependence of σ_{xx} under the zero field from 2 to 50 K, shown in Figure S9a,b, reveals that conductivity decreases with the increasing temperatures, remaining on the order of 10^6 at low temperatures. Subsequently, we thus extract the carrier mobilities by using the semiclassical Drude model,[14,35] $\sigma_{xx}(B) = \frac{n_h e\mu_h}{1+\mu_h^2B^2} + \frac{n_e e\mu_e}{1+\mu_e^2B^2}$, $\sigma_{xy}(B) = \frac{n_h e\mu_h^2 B}{1+\mu_h^2B^2} - \frac{n_e e\mu_e^2 B}{1+\mu_e^2B^2}$, showing good agreement with the experimental data (black) measured at 2, 10, 15, and 30 K (Figure S9c−f). The extracted carrier mobility of electrons and holes is about 8761 $cm^2 V^{-1} s^{-1}$ and 2187 $cm^2 V^{-1} s^{-1}$ at 2 K, respectively, and both mobilities decrease with the increasing temperature, as shown in Figure 3e. The carrier mobility in our $Ni_3In_2Se_2$ nanoflakes shows a larger value, as compared to reported magnetic topological semimetals (Figure 3f), such as $Co_3Sn_2S_2$ (2600 $cm^2 V^{-1} s^{-1}$), YV_6Sn_6 (6900 $cm^2 V^{-1} s^{-1}$), $MnBi_2Te_4$ (3110 $cm^2 V^{-1} s^{-1}$), and Co_2MnGa (35 $cm^2 V^{-1} s^{-1}$).[35−41] Remarkably, the carrier mobility of $Ni_3In_2Se_2$ is several times higher than that of the structurally similar $Co_3Sn_2S_2$,.[14] The outstanding transport characteristics of $Ni_3In_2Se_2$ offer an ideal platform for the development of high-speed electronic and optoelectronic devices.

Subsequently, we focus on the study of the in-plane magnetotransport properties of the $Ni_3In_2Se_2$ nanoflake. The planar Hall effect and anisotropic magnetoresistance of $Ni_3In_2Se_2$ were measured with the magnetic field applied in the x−y plane (ab-plane of the crystal). The inset of Figure 4b shows a typical PHE measurement setup, where the magnetic field B rotates in the ab-plane while the longitudinal and transverse voltages are measured, corresponding to changes in the AMR and planar Hall resistivity, respectively. The angular dependence of the AMR and planar Hall resistivity can be given by the expressions,[19,20,42,43]

$$\rho_{xy}^{\mathrm{PHE}} = -\Delta\rho_{xy} \sin\varphi \cos\varphi + b \tag{1}$$

$$\mathrm{AMR}_{\mathrm{ratio}} = \left(\frac{\rho_{xx,\varphi} - \rho_{xx,\perp}}{\rho_{xx,\perp}}\right) \times 100\% \tag{2}$$

$$\rho_{xx} = \rho_{\perp} - \Delta\rho_{xy} \cos^2\varphi \tag{3}$$

where $\Delta\rho_{xy} = \rho_{\perp} - \rho_{//}$ refers to resistivity anisotropy induced by the chiral anomaly; $\rho_{\perp}$ and $\rho_{//}$ are regarded as the longitudinal resistivity when B is perpendicular or parallel to I, respectively. Figure 4a shows the angular dependence of the planar Hall resistivity measured at 2 K for B varying from 0.5 to 9 T, showing that the amplitude gradually increases with the increasing magnetic fields, with a large ρ_{xy}^{PHE} value of 1.28 $\mu\Omega\cdot$cm under 9 T. The field-dependent $\Delta\rho_{xy}$ extracted by fitting ρ_{xy}^{PHE} under different fields exhibits a power-law dependence with an exponent of 1.073 (Figure 4b). Theoretical calculations indicate that if the PHE signal purely derives from chiral anomaly, $\Delta\rho_{xy}$ should be proportional to B^2.[44] The temperature-dependent amplitude of the planar Hall effect was further analyzed under a magnetic field of 9 T. The angular dependence of PHE under 9 T for the temperature varying from 2 to 100 K (Figure 4c) shows that the amplitude gradually decreases with increasing temperature. The extracted $\Delta\rho_{xy}$ obtained by fitting ρ_{xy}^{PHE} decreases as the temperature increases, with observable values persisting up to 100 K (Figure S10a).

Typically, three main microscopic mechanisms are likely to contribute to the PHE. One mechanism involves spin-dependent scattering effects in ferromagnets, which result from the rotation of magnetization relative to the current direction, altering the scattering rate.[45] Another mechanism is anisotropic orbital magnetoresistance arising from Fermi-pocket anisotropy.[19] A third mechanism is the chiral anomaly, which is related to the chiral charge pumping in Weyl semimetals.[46] As the magnetic field is parallel to the current, the longitudinal resistivity of $Ni_3In_2Se_2$ shows a positive MR (Figure 3a), which contrasts with the negative magnetoresistance (NMR) expected from the chiral anomaly. While the chiral anomaly predicts $\rho_{\perp}$ remains nearly constant and $\rho_{//}$ decreases with the increasing magnetic fields,[47,48] $\rho_{\perp}$ is observed to increase with the fields (Figure S10b,c), deviating from this expected behavior. Furthermore, the anisotropic orbital magnetoresistance will lead to $\rho_{\perp} > \rho_{//} > 0$, which is consistent with our observed results, in which if there are multiple Fermi pockets or the Fermi pockets have the complex shape, scattering time, effective mass, and mobility can vary significantly as carriers move in different directions, leading to the anisotropic orbital MR, which contributes to PHE. Therefore, based on the field-induced ferromagnetism of $Ni_3In_2Se_2$, its PHE primarily arises from the complex interaction between the spin scattering and orbital MR.

Beyond the microscopic origin of the PHE, an equally intriguing feature is the rotational symmetry distortion observed in the angular dependence of the in-plane AMR. At 2 and 10 K, the AMR progressively deviates from a simple 2-fold symmetry as the magnetic field increases from 0.5 to 9 T. The angular AMR profile evolves from a nearly symmetric 2-fold "peanut-like" shape into a progressively distorted pattern, characterized by broadened maxima and sharpened minima at higher fields, ultimately reaching a maximum AMR ratio of 41% at 9 T (Figures 4d,e, S10d, and S11a,b). Moreover, with increasing temperature, the AMR gradually weakens, and the pronounced angular distortions observed at 5 and 9 T progressively smooth out, with the peanut-like profile gradually rounding off toward a smooth, nearly symmetric 2-fold form (Figures 4f,g and S11c,d). This field-induced distortion, which already emerges at relatively low magnetic fields and intensifies with the increasing field strength, indicates the involvement of higher-order contributions and reflects a superposition of second- and higher-order angular components. The AMR curves measured at 2 K under magnetic fields from 0.5 to 9 T were subjected to the Fourier analysis (Figure 4h), revealing distinct peaks in the Fourier amplitude (AFT) at 180° (2-fold, C_2 symmetry), 90° (4-fold, C_4 symmetry), and 60° (6-fold, C_6 symmetry), with the higher-order peaks becoming increasingly pronounced as the magnetic field increases, confirming that the angular dependence of the AMR arises from the superposition of multiple symmetry components. As the temperature rises, the 4-fold and 6-fold components gradually weaken, leaving the 2-fold component as the dominant contribution (Figures 4i and S12a−c). As shown in the three-dimensional planform of AMR at 2 K under different fields from 0.5 to 9 T (Figure S12d), a progressively distorted AMR, reflecting the breaking

Downloaded from pubs.acs.org/ancac3/article-pdf/20/30/21316/66049429/acsnano.6c06737.pdf by INST OF PHYSICS user on 30 September 2026

https://doi.org/10.1021/acsnano.6c06737
ACS Nano 2026, 20, 21316−21326

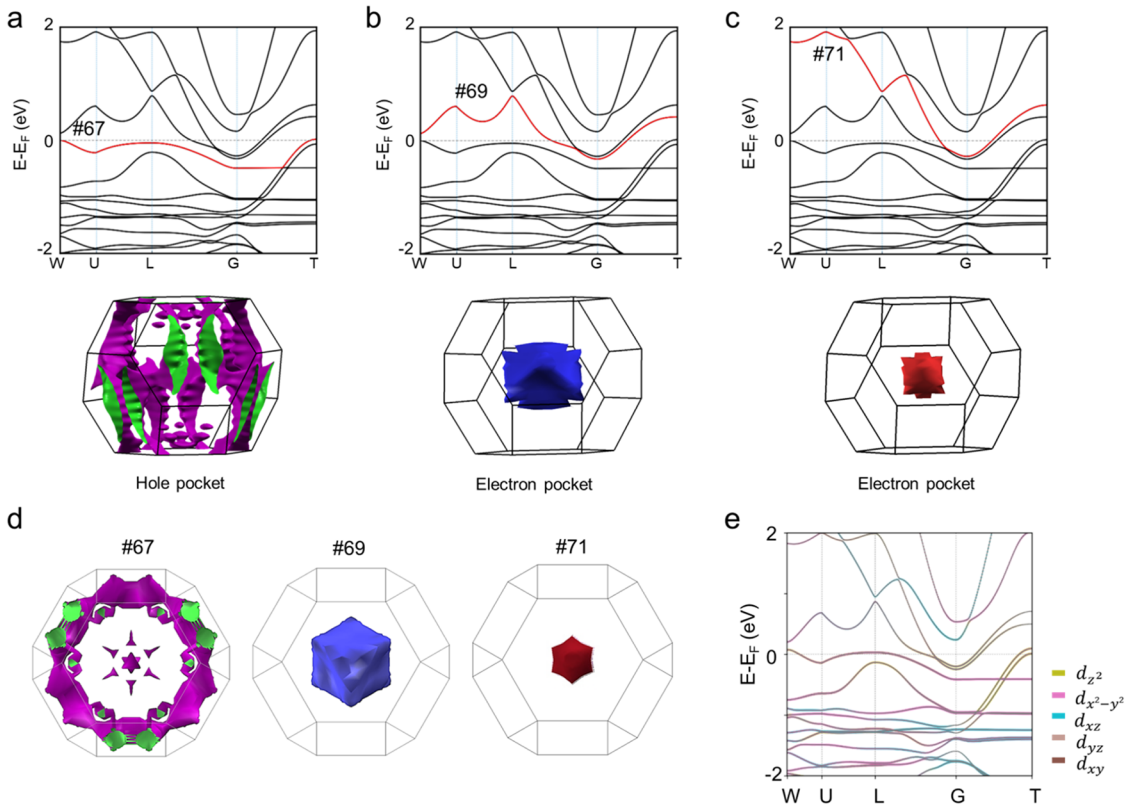

Figure 5. Calculated Fermi surfaces and projected band structure for the $Ni_3In_2Se_2$ crystals. (a−c) Calculated band structures (the upper ones marked by red lines) and corresponding three-dimensional Fermi surfaces (the lower ones) of $Ni_3In_2Se_2$, where band 67 is the hole pocket, while bands 69 and 71 represent the electron pockets. (d) Projection of the three-dimensional Fermi surfaces of bands 67, 69, and 71 onto the *ab*-plane. (e) Plots of the Ni 3*d* orbital-projected band structure for $Ni_3In_2Se_2$.

of conventional 2-fold rotational symmetry, emerges above 2 T and persists up to 9 T. Moreover, the temperature evolution of the three-dimensional AMR map (Figure S12e) reveals that the higher-order AMR signals will gradually disappear with increasing temperature, and the normal 2-fold AMR dominates at high temperatures. The distorted AMR signals persist up to 20 K under both 5 and 9 T, indicating that the high-order contributions remain robust over this temperature range. Figure S13 shows the three-dimensional planform of the AMR effect at 10 and 20 K under magnetic fields ranging from 0.5 to 9 T, where the distorted high-order AMR signals gradually weaken as the temperature increases.

To further analyze this unconventional behavior, the AMR curves were fitted using the following expression to quantify the contributions of each symmetry component:[49]

$$\mathrm{AMR}(\varphi) = C_0 + C_2 \cos(2(\varphi + \psi_1)) + C_4 \cos(4(\varphi + \psi_2)) + C_6 \cos(6(\varphi + \psi_3)) \quad (4)$$

Here, C_0 is a constant, while the terms $C_2 \cos(2\varphi)$, $C_4 \cos(4\varphi)$, and $C_6 \cos(6\varphi)$ represent contributions from the 2-fold, 4-fold, and 6-fold symmetry components, respectively, and ψ_1, ψ_2, and ψ_3 denote the phase angles of the 2-fold, 4-fold, and 6-fold components of the anisotropic resistivity. Figure S14 shows the fitting results, from which the amplitudes of C_2, C_4, and C_6 at various temperatures and magnetic fields can be extracted, representing the three AMR components. The proportion of the C_2 signal decreases from 95% to 82% as the magnetic field increases to 2 T, while the C_4 and C_6 components increase significantly, with C_4 slightly decreasing at higher fields (Figure S15a−c). For a detailed analysis of the temperature dependence, the amplitudes of C_2, C_4, and C_6 were obtained over a temperature range of 2 to 100 K under 9 T (Figure S15d−f). As the temperature increases from 2 to 100 K, the proportion of the C_2 signal rises rapidly from 83% to 99%, while the C_4 and C_6 components gradually diminish and almost vanish around 100 K, indicating that the 2-fold AMR becomes dominant at elevated temperatures.

To further explore the field-induced unconventional AMR effect, we performed DFT calculations of the Fermi surfaces and projected band structure of $Ni_3In_2Se_2$. Figure 5a−c displays the band structures, showing three bands labeled 67, 69, and 71 that cross the Fermi level (highlighted in red). The corresponding theoretical Fermi surfaces of $Ni_3In_2Se_2$ are shown in the lower panels of Figure 5a−c, revealing three distinct pockets: two electron pockets with a petal-like geometry and one hole pocket with a spindle-like shape. This coexistence of electron and hole pockets explains the nonlinear Hall behavior observed in Figure 3c. By projecting the three-dimensional Fermi surfaces onto the $k_z = 0$ plane (Figure 5d), it is evident that the Fermi surfaces exhibit an overall 6-fold symmetry, while locally showing stretching, distortion, and phase shifts, forming a 6-fold skeleton with local distortions and explaining why the Fourier spectra display not only the 6-fold component from the Fermi surface symmetry but also an additional 4-fold contribution. Moreover, the Ni 3d orbitals (Figures 5e and S16), particularly d_{xz}, d_{yz}, d_{xy}, and $d_{x^2-y^2}$, exhibit a cloverleaf-like spatial distribution. Such orbital symmetry strongly influences the surrounding electronic states and their scattering pathways. Consequently, under external

https://doi.org/10.1021/acsnano.6c06737
ACS Nano 2026, 20, 21316−21326

Downloaded from pubs.acs.org/ancac3/article-pdf/20/30/21316/66049429/acsnano.6c06737.pdf by INST OF PHYSICS user on 30 September 2026

magnetic fields, this anisotropic orbital character induces a directional dependence in the charge transport, giving rise to the observed 4-fold AMR effect.[50,51] We further analyze why the relative contribution of higher-order signals increases with the increasing magnetic fields. Spin−orbit coupling (SOC) renders orbital states sensitive to the magnetization direction, with the resulting orbital selectivity inducing a strongly anisotropic $\tau(k)$ distribution that affects the conductivity tensor in the Boltzmann formalism[52]

$$\sigma_{ij} = \frac{e^2}{(2\pi)^3} \int \tau^k v_i^k v_j^k \frac{\mathrm{d}S}{|\nabla_k E^k|} \tag{5}$$

Here, $v(k)$ denotes the group velocity of electrons at wave vector k, determined by the gradient of the band dispersion, while $\tau(k)$ represents the relaxation time. The increasing distortion of the angular dependence with the magnetic field is primarily attributed to the enhanced contribution of higher-order symmetry components, which may arise from three interrelated factors. One is that high magnetic fields suppress spin fluctuations, leading to a more coherent magnetization state and stronger coupling to orbital degrees of freedom, thereby amplifying the $\tau(k)$ variations associated with orbital anisotropy. Another involves the combination of Zeeman splitting and field-induced orbital hybridization, which alters the band energy sequence and hybridization strength, significantly reshaping the Fermi surface curvature and group velocity distribution and resulting in enhanced Fermi surface distortions. A third arises from modifications of the density of states near the Fermi level, which affect the directional scattering probability of conduction electrons and enhance the contributions of higher-order symmetry components associated with the underlying Fermi surface symmetry (C_6) and orbital distribution (C_4), as reflected in the stronger 4-fold and 6-fold components in the Fourier spectra.

CONCLUSIONS

In summary, we have successfully synthesized hexagonal-shaped $Ni_3In_2Se_2$ nanoflakes by using an iterative-CVT approach with the polycrystal granules as source materials. Magnetic measurements, together with theoretical calculations, indicate that $Ni_3In_2Se_2$ crystals host a canted ferromagnetic ground state with a field-induced out-of-plane ferromagnetic component. Besides, the high-quality $Ni_3In_2Se_2$ nanoflake exhibits excellent transport properties, including the large magnetoresistance, significant out-of-plane AMR, and high carrier mobility of approximately 590% under 7 T, 200% under 5 T, and 8761 $cm^2\ V^{-1}\ s^{-1}$ at 2 K, respectively. Furthermore, PHE observed in the $Ni_3In_2Se_2$ nanoflakes arises from the complex interplay of the field-induced ferromagnetism and orbital magnetoresistance with the in-plane AMR reaching a maximum of 41% under 9 T. Interestingly, $Ni_3In_2Se_2$ exhibits pronounced in-plane transport anisotropy with magnetic-field-induced rotational symmetry distortion at low temperatures, as revealed by the distorted AMR curves that reflect the superposition of 2-fold, 4-fold, and 6-fold symmetry components, likely arising from the field-induced orbital polarization and field-enhanced Fermi surface anisotropy. Our work establishes an effective approach for the growth of high-quality kagome semimetal materials and contributes to the development of high-performance electronic and spintronic devices.

METHODS

Growth of the $N_3In_2Se_2$ Nanoflakes

The kagome-lattice $N_3In_2Se_2$ nanoflakes were successfully synthesized using a chemical vapor transport method, with single-crystal granules serving as the source materials. First, single-crystal $N_3In_2Se_2$ samples with irregular shapes were prepared using the self-flux method, where the raw materials of Ni, In, and Se were mixed in a molar ratio of 3:2:2, placed in a crucible, and sealed in a quartz tube under high vacuum using a high-temperature flame gun. The quartz tube was slowly heated for 48 h to 1050 °C and then kept constant at that temperature for 24 h and cooled to 600 °C at a rate of 10 °C/h. Subsequently, the growth of the hexagonal $Ni_3In_2Se_2$ nanoflakes was performed in a temperature gradient from 1000 to 900 °C for about a week, with the single-crystal granules as a vapor source and halide as a transport agent. The iterative-CVT approach yields significantly higher-quality single-crystalline $Ni_3In_2Se_2$ hexagonal flakes than the conventional self-flux method due to three key advantages. First, the nonvolatile NH_4Cl provides a clean high-vacuum environment and stable growth conditions, promoting preferential growth and minimizing contamination. Second, the use of $Ni_3In_2Se_2$ crystal granules as precursors helps preserve the stoichiometric balance of Ni, In, and Se while avoiding undesirable side reactions. Third, NH_4Cl enables more efficient mass transport, ensuring a sufficient precursor supply and continuous crystal growth. Collectively, these advantages facilitate the growth of high-quality $Ni_3In_2Se_2$ hexagonal flakes with the enhanced crystallinity and reduced structural defects.

Sample Characterization

XRD patterns were collected using a Rigaku SmartLab SE X-ray diffractometer with Cu Kα radiation (λ = 0.15418 nm) at room temperature. Single-crystal diffraction patterns and rocking curves were taken by a Bruker D8 Venture. Scanning electron microscopy (SEM) and X-ray energy-dispersive spectroscopy (EDS) were performed using a HITACHI S5000 with an energy-dispersive analysis system, Bruker XFlash 6|60. Magnetization measurements were carried out on oriented crystals with the magnetic field applied along the c-axis using a vibrating sample magnetometer (MPMS 3, Quantum Design). Both in-plane electrical resistivity and Hall resistivity data were collected on a Quantum Design Physical Properties Measurement System (PPMS).

DFT Calculations

First-principles calculations are performed in the framework of density functional theory (DFT), as implemented in the Vienna Ab initio Simulation Package (VASP). The projected-augmented-wave (PAW) pseudopotentials are applied to describe the electron−ion interaction with a plane-wave cutoff of 400 eV. Here, Ni-$4s^23d^8$, In-$4d^{10}5s^25p$, and Se-$3d^{10}4s^24p^4$ electron states are treated as valence electrons. The Perdew−Burke−Ernzerhof (PBE) functional is used to deal with the electron exchange−correlation potentials. The primitive cell of $Ni_3In_2Se_2$ is considered in our calculations, and a 10 × 10 × 10 k-point grid is applied. The atomic position and lattice parameters are fully relaxed until the residual force on each atom is less than 0.01 eV·$Å^{-1}$.

ASSOCIATED CONTENT

Data Availability Statement

Data measured or analyzed during this study are available from the corresponding author upon reasonable request.

Supporting Information

The Supporting Information is available free of charge at https://pubs.acs.org/doi/10.1021/acsnano.6c06737.

Additional details on the crystal growth and structural characterization, nanoflake transfer process, magnetic properties, magnetotransport measurements, two-carrier model analysis, in-plane anisotropic magnetoresistance and planar Hall effect, Fourier transform and symmetry

Downloaded from pubs.acs.org/ancac3/article-pdf/20/30/21316/66049429/acsnano.6c06737.pdf by INST OF PHYSICS user on 30 September 2026

https://doi.org/10.1021/acsnano.6c06737
ACS Nano 2026, 20, 21316−21326

component analyses of the AMR, and projected band structures of Ni 3d orbitals are provided in Figures S1–S16 (PDF)

AUTHOR INFORMATION

Corresponding Authors

Jinbo Pan – *Beijing National Center for Condensed Matter Physics and Institute of Physics, Chinese Academy of Sciences, Beijing 100190, P. R. China;* orcid.org/0000-0003-2612-8232; Email: jbpan@iphy.ac.cn

Jun He – *Division of Functional Material Research, Central Iron & Steel Research Institute, Beijing 100081, P. R. China;* Email: hejun@cisri.com.cn

Haitao Yang – *Beijing National Center for Condensed Matter Physics and Institute of Physics, Chinese Academy of Sciences, Beijing 100190, P. R. China; School of Physical Sciences, University of Chinese Academy of Sciences, Beijing 100049, P. R. China;* orcid.org/0000-0003-4304-9835; Email: htyang@iphy.ac.cn

Authors

Senhao Lv – *Beijing National Center for Condensed Matter Physics and Institute of Physics, Chinese Academy of Sciences, Beijing 100190, P. R. China*

Hui Guo – *Beijing National Center for Condensed Matter Physics and Institute of Physics, Chinese Academy of Sciences, Beijing 100190, P. R. China;* orcid.org/0000-0002-2088-0522

Yuhui Li – *Beijing National Center for Condensed Matter Physics and Institute of Physics, Chinese Academy of Sciences, Beijing 100190, P. R. China*

Guojing Hu – *Beijing National Center for Condensed Matter Physics and Institute of Physics, Chinese Academy of Sciences, Beijing 100190, P. R. China*

Guolin Wan – *Beijing National Center for Condensed Matter Physics and Institute of Physics, Chinese Academy of Sciences, Beijing 100190, P. R. China*

Ruwen Wang – *Beijing National Center for Condensed Matter Physics and Institute of Physics, Chinese Academy of Sciences, Beijing 100190, P. R. China*

Guoyu Xian – *Beijing National Center for Condensed Matter Physics and Institute of Physics, Chinese Academy of Sciences, Beijing 100190, P. R. China*

Xinwei Yi – *Beijing National Center for Condensed Matter Physics and Institute of Physics, Chinese Academy of Sciences, Beijing 100190, P. R. China*

Zhen Zhao – *Beijing National Center for Condensed Matter Physics and Institute of Physics, Chinese Academy of Sciences, Beijing 100190, P. R. China*

Nan Si – *Multidisciplinary Center for Infrastructure Engineering, Shenyang University of Technology, Shenyang, Liaoning 110870, P. R. China*

Ke Zhu – *Beijing National Center for Condensed Matter Physics and Institute of Physics, Chinese Academy of Sciences, Beijing 100190, P. R. China*

Yechao Han – *School of Physical Sciences, University of Chinese Academy of Sciences, Beijing 100049, P. R. China*

Lihong Bao – *Beijing National Center for Condensed Matter Physics and Institute of Physics, Chinese Academy of Sciences, Beijing 100190, P. R. China;* orcid.org/0000-0002-2942-892X

Xiao Lin – *School of Physical Sciences, University of Chinese Academy of Sciences, Beijing 100049, P. R. China;* orcid.org/0000-0002-2490-4691

Shixuan Du – *Beijing National Center for Condensed Matter Physics and Institute of Physics, Chinese Academy of Sciences, Beijing 100190, P. R. China;* orcid.org/0000-0001-9323-1307

Hong-Jun Gao – *Beijing National Center for Condensed Matter Physics and Institute of Physics, Chinese Academy of Sciences, Beijing 100190, P. R. China; School of Physical Sciences, University of Chinese Academy of Sciences, Beijing 100049, P. R. China;* orcid.org/0000-0002-6766-0623

Complete contact information is available at: https://pubs.acs.org/10.1021/acsnano.6c06737

Author Contributions

[⊥]S.H.L. and H.G. contributed equally to this work. H.-J.G. designed the project. H.T.Y. and S.H.L. prepared the samples. S.H.L., J.H., and H.T.Y. performed the magnetization measurements. S.H.L., H.G., G.J.H., R.W.W., G.Y.X., Z.Z., K.Z., Y.C.H., L.H.B., X.L., and H.T.Y. performed the transport experiments. Y.H.L., G.L.W., X.W.Y., N.S., J.B.P., and S.X.D. performed DFT calculations. All authors participated in the data analysis and manuscript writing.

Notes

The authors declare no competing financial interest.

ACKNOWLEDGMENTS

The work was supported by grants from the National Key Research and Development Projects of China (2022YFA1204100, 2024YFA1207800), the National Natural Science Foundation of China (62488201, 52572188, 92580202, U23A6015), the Strategic Priority Research Program of Chinese Academy of Sciences (XDB1700000, XDB1710000), the Innovation Program of Quantum Science and Technology (2021ZD0302700), the Chinese Academy of Sciences (YSBR-003, YSBR-053), and the China Postdoctoral Science Foundation (E5BK081).

REFERENCES

(1) Wang, Y. J.; Wu, H.; McCandless, G. T.; Chan, J. Y.; Ali, M. N. Quantum States and Intertwining Phases in Kagome Materials. *Nat. Rev. Phys.* **2023**, *5*, 635–658.

(2) Bernevig, B. A.; Felser, C.; Beidenkopf, H. Progress and Prospects in Magnetic Topological Materials. *Nature* **2022**, *603*, 41–51.

(3) Li, X. K.; Koo, J.; Zhu, Z. W.; Behnia, K.; Yan, B. H. Field-Linear Anomalous Hall Effect and Berry Curvature Induced by Spin Chirality in the Kagome Antiferromagnet Mn_3Sn. *Nat. Commun.* **2023**, *14*, No. 1642.

(4) Yin, J. X.; Lian, B.; Hasan, M. Z. Topological Kagome Magnets and Superconductors. *Nature* **2022**, *612*, 647–657.

(5) Ye, L. D.; Kang, M. G.; Liu, J. W.; von Cube, F.; Wicker, C. R.; Suzuki, T.; Jozwiak, C.; Bostwick, A.; Rotenberg, E.; Bell, D. C.; Fu, L.; Comin, R.; Checkelsky, J. G. Massive Dirac Fermions in a Ferromagnetic Kagome Metal. *Nature* **2018**, *555*, 638–642.

(6) Yin, J.-X.; Ma, W. L.; Cochran, T. A.; Xu, X. T.; Zhang, S. S.; Tien, H.-J.; Shumiya, N.; Cheng, G. M.; Jiang, K.; Lian, B.; Song, Z. D.; Chang, G. Q.; Belopolski, I.; Multer, D.; Litskevich, M.; Cheng, Z.-J.; Yang, X. P.; Swidler, B.; Zhou, H. B.; Lin, H.; Neupert, T.; Wang, Z. Q.; Yao, N.; Chang, T.-R.; Jia, S.; Hasan, M. Z. Quantum-Limit Chern Topological Magnetism in $TbMn_6Sn_6$. *Nature* **2020**, *583*, 533–536.

Downloaded from pubs.acs.org/ancac3/article-pdf/20/30/21316/66049429/acsnano.6c06737.pdf by INST OF PHYSICS user on 30 September 2026

(7) Morali, N.; Batabyal, R.; Nag, P. K.; Liu, E. K.; Xu, Q. A.; Sun, Y.; Yan, B. H.; Felser, C.; Avraham, N.; Beidenkopf, H. Fermi-Arc Diversity on Surface Terminations of the Magnetic Weyl Semimetal $Co_3Sn_2S_2$. *Science* **2019**, *365*, 1286−1291.
(8) Tang, E.; Mei, J. W.; Wen, X. G. High-Temperature Fractional Quantum Hall States. *Phys. Rev. Lett.* **2011**, *106*, No. 236802.
(9) Wu, M.-X.; Wei, Y.-H.; Ma, D.-S.; Wang, P.; Gao, N.; Wu, S.-Y.; Kuang, M.-Q. In-Plane Canted Ferromagnetism, Intrinsic Weyl Fermions, and Large Anomalous Hall Effect in the Kagome Semimetal $Rh_3Sn_2S_2$. *Phys. Rev. B* **2023**, *108*, No. 174430.
(10) Muechler, L.; Liu, E. K.; Gayles, J.; Xu, Q. N.; Felser, C.; Sun, Y. Emerging Chiral Edge States from the Confinement of a Magnetic Weyl Semimetal in $Co_3Sn_2S_2$. *Phys. Rev. B* **2020**, *101*, No. 115106.
(11) Wang, Y.-C.; Zhang, X.-F.; Pollmann, F.; Cheng, M.; Meng, Z. Y. Quantum Spin Liquid with Even Ising Gauge Field Structure on Kagome Lattice. *Phys. Rev. Lett.* **2018**, *121*, No. 057202.
(12) Zhang, Z.; You, J.-Y.; Ma, X.-Y.; Gu, B.; Su, G. Kagome Quantum Anomalous Hall Effect with High Chern Number and Large Band Gap. *Phys. Rev. B* **2021**, *103*, No. 014410.
(13) Nakatsuji, S.; Kiyohara, N.; Higo, T. Large Anomalous Hall Effect in a Non-Collinear Antiferromagnet at Room Temperature. *Nature* **2015**, *527*, 212−215.
(14) Liu, E. K.; Sun, Y.; Kumar, N.; Muechler, L.; Sun, A.; Jiao, L.; Yang, S.-Y.; Liu, D.; Liang, A. J.; Xu, Q. N.; Kroder, J.; Süß, V.; Borrmann, H.; Shekhar, C.; Wang, Z. S.; Xi, C. Y.; Wang, W. H.; Schnelle, W.; Wirth, S.; Chen, Y. L.; Goennenwein, S. T. B.; Felser, C. Giant Anomalous Hall Effect in a Ferromagnetic Kagome-Lattice Semimetal. *Nat. Phys.* **2018**, *14*, 1125−1131.
(15) Rout, P. K.; Madduri, P. V. P.; Manna, S. K.; Nayak, A. K. Field-Induced Topological Hall Effect in the Noncoplanar Triangular Antiferromagnetic Geometry of Mn_3Sn. *Phys. Rev. B* **2019**, *99*, No. 094430.
(16) Ma, J. J.; Shi, C. F.; Cao, Y. T.; Zhang, Y. W.; Li, Y. Z.; Liao, J. X.; Wang, J. L.; Jiao, W. H.; Guo, H. J.; Xu, C. C.; Cao, S. X.; Dai, J. H.; Bao, J.-K.; Li, Y. K. Anisotropic Transport Properties and Topological Hall Effect in the Annealed Kagome Antiferromagnet FeGe. *Sci. China, Ser. G:Phys., Mech. Astron.* **2025**, *68*, No. 237412.
(17) Ma, J. J.; Liao, J. X.; Li, Y. Z.; Zhang, Y. W.; Wang, J. L.; Bao, J.-K.; Sun, Y.; Jia, S.; Li, Y. K. Large Room Temperature Anomalous Nernst Effect Coupled with Topological Nernst Effect from Incommensurate Spin Structure in a Kagome Antiferromagnet. *Adv. Sci.* **2026**, *13*, No. e22151.
(18) Sharma, V.; Nepal, R.; Budhani, R. C. Planar Hall Effect and Anisotropic Magnetoresistance in Thin Films of the Chiral Antiferromagnet Mn_3Sn. *Phys. Rev. B* **2023**, *108*, No. 144435.
(19) Yang, S.-Y.; Noky, J.; Gayles, J.; Dejene, F. K.; Sun, Y.; Dörr, M.; Skourski, Y.; Felser, C.; Ali, M. N.; Liu, E. K.; Parkin, S. S. P. Field-Induced Anomalous Hall Conductivity and Planar Hall Effect in $Co_3Sn_2S_2$ Nanoflakes. *Nano Lett.* **2020**, *20*, 7860−7867.
(20) Ma, X.; Huang, M.; Wang, S. S.; Liu, P.; Zhang, Y.; Lu, Y. L.; Xiang, B. Anisotropic Magnetoresistance and Planar Hall Effect in Layered Room-Temperature Ferromagnet $Cr_{1.2}Te_2$. *ACS Appl. Electron. Mater.* **2023**, *5*, 2838−2844.
(21) Burkov, A. A. Giant Planar Hall Effect in Topological Metals. *Phys. Rev. B* **2017**, *96*, No. 041110.
(22) Li, H.; Wang, H.-W.; He, H. T.; Wang, J. N.; Shen, S.-Q. Giant Anisotropic Magnetoresistance and Planar Hall Effect in the Dirac Semimetal Cd_3As_2. *Phys. Rev. B* **2018**, *97*, No. 201110(R).
(23) Ali, M. N.; Schoop, L. M.; Garg, C.; Lippmann, J. M.; Lara, E.; Lotsch, B.; Parkin, S. S. P. Butterfly Magnetoresistance, Quasi-2D Dirac Fermi Surface and Topological Phase Transition in ZrSiS. *Sci. Adv.* **2016**, *2*, No. e1601742.
(24) Jo, Y. J.; Park, J.; Lee, G.; Eom, M. J.; Choi, E. S.; Shim, J. H.; Kang, W.; Kim, J. S. Valley-Polarized Interlayer Conduction of Anisotropic Dirac Fermions in $SrMnBi_2$. *Phys. Rev. Lett.* **2014**, *113*, No. 156602.
(25) Chen, J.; Li, H.; Guo, T.; Chen, P.; Zheng, D.; Yu, G.; Lau, Y.-C.; Xi, X.; Wang, W. Anomalous Anisotropic Magnetoresistance in the Topological Semimetal HoPtBi. *NPG Asia Mater.* **2023**, *15*, No. 34.
(26) Wang, J.; Deng, J.; Liang, X.; Gao, G.; Ying, T.; Tian, S.; et al. Spin-Flip-Driven Giant Magnetotransport in A-Type Antiferromagnet NaCrTe2. *Phys. Rev. Mater.* **2021**, *5*, No. L091401.
(27) Xu, J.; Wu, F.; Bao, J.-K.; Han, F.; Xiao, Z. L.; Martin, I.; Lyu, Y.-Y.; Wang, Y.-L.; Chung, D. Y.; Li, M.; Zhang, W.; Pearson, J. E.; Jiang, J. S.; Kanatzidis, M. G.; Kwok, W.-K. Orbital-Flop Induced Magnetoresistance Anisotropy in Rare Earth Monopnictide CeSb. *Nat. Commun.* **2019**, *10*, No. 2875.
(28) Lyu, Y.-Y.; Han, F.; Xiao, Z.-L.; Xu, J.; Wang, Y.-L.; Wang, H.-B.; Bao, J.-K.; Chung, D. Y.; Li, M.; Martin, I.; Welp, U.; Kanatzidis, M. G.; Kwok, W.-K. Magnetization-Governed Magnetoresistance Anisotropy in the Topological Semimetal CeBi. *Phys. Rev. B* **2019**, *100*, No. 180407(R).
(29) Hodovanets, H.; Eckberg, C. J.; Campbell, D. J.; Eo, Y.; Zavalij, P. Y.; Piccoli, P.; Metz, T.; Kim, H.; Higgins, J. S.; Paglione, J. Anomalous Symmetry Breaking in the Weyl Semimetal CeAlGe. *Phys. Rev. B* **2022**, *106*, No. 235102.
(30) Wang, C.; Seinige, H.; Cao, G.; Zhou, J. S.; Goodenough, J. B.; Tsoi, M. Anisotropic Magnetoresistance in Antiferromagnetic Sr2IrO4. *Phys. Rev. X* **2014**, *4*, No. 041034.
(31) Akatsuka, S.; Esser, S.; Okumura, S.; Yambe, R.; Yamada, R.; Hirschmann, M. M.; Aji, S.; White, J. S.; Gao, S.; Onuki, Y.; Arima, T.-H.; Nakajima, T.; Hirschberger, M. Non-Coplanar Helimagnetism in the Layered van der Waals Metal $DyTe_3$. *Nat. Commun.* **2024**, *15*, No. 4291.
(32) Sung, N. H.; Ronning, F.; Thompson, J. D.; Bauer, E. D. Magnetic Phase Dependence of the Anomalous Hall Effect in Mn_3Sn Single Crystals. *Appl. Phys. Lett.* **2018**, *112*, No. 132406.
(33) Han, F.; Xu, J.; Botana, A. S.; Xiao, Z. L.; Wang, Y. L.; Yang, W. G.; Chung, D. Y.; Kanatzidis, M. G.; Norman, M. R.; Crabtree, G. W.; Kwok, W. K. Separation of Electron and Hole Dynamics in the Semimetal LaSb. *Phys. Rev. B* **2017**, *96*, No. 125112.
(34) Petrova, A. E.; Sobolevskiy, O. A.; Stishov, S. M. Magnetoresistance and Kohler Rule in the Topological Chiral Semimetal CoSi. *Phys. Rev. B* **2023**, *107*, No. 085136.
(35) Tanaka, M.; Fujishiro, Y.; Mogi, M.; Kaneko, Y.; Yokosawa, T.; Kanazawa, N.; Minami, S.; Koretsune, T.; Arita, R.; Tarucha, S.; Yamamoto, M.; Tokura, Y. Topological Kagome Magnet $Co_3Sn_2S_2$ Thin Flakes with High Electron Mobility and Large Anomalous Hall Effect. *Nano Lett.* **2020**, *20*, 7476−7481.
(36) Fang, H. W.; Lyu, M.; Su, H.; Yuan, J.; Li, Y. W.; Xu, L. X.; Liu, S.; Wei, L. Y.; Liu, X. Q.; Yang, H. F.; Yao, Q.; Wang, M. X.; Guo, Y. F.; Shi, W. J.; Chen, Y. L.; Liu, E. K.; Liu, Z. K. Record-High Mobility and Extreme Magnetoresistance on Kagome-Lattice in Compensated Semimetal $Ni_3In_2S_2$. *Sci. China Mater.* **2023**, *66*, 2032−2038.
(37) Pokharel, G.; Teicher, S. M. L.; Ortiz, B. R.; Sarte, P. M.; Wu, G.; Peng, S. T.; He, J. F.; Seshadri, R.; Wilson, S. D. Electronic Properties of the Topological Kagome Metals YV_6Sn_6 and GdV_6Sn_6. *Phys. Rev. B* **2021**, *104*, No. 235139.
(38) Hirschberger, M.; Kushwaha, S.; Wang, Z. J.; Gibson, Q.; Liang, S. H.; Belvin, C. A.; Bernevig, B. A.; Cava, R. J.; Ong, N. P. The Chiral Anomaly and Thermopower of Weyl Fermions in the Half-Heusler GdPtBi. *Nat. Mater.* **2016**, *15*, 1161−1165.
(39) Liu, C.; Wang, Y. C.; Yang, M.; Mao, J. H.; Li, H.; Li, Y. X.; Li, J. H.; Zhu, H. P.; Wang, J. F.; Li, L.; Wu, Y.; Xu, Y.; Zhang, J. S.; Wang, Y. Y. Magnetic-Field-Induced Robust Zero Hall Plateau State in $MnBi_2Te_4$ Chern Insulator. *Nat. Commun.* **2021**, *12*, No. 4647.
(40) Belopolski, I.; Manna, K.; Sanchez, D. S.; Chang, G. Q.; Ernst, B.; Yin, J. X.; Zhang, S. T. S.; Cochran, T.; Shumiya, N.; Zheng, H.; Singh, B.; Bian, G.; Multer, D.; Litskevich, M.; Zhou, X. T.; Huang, S.-M.; Wang, B. K.; Chang, T.-R.; Xu, S.-Y.; Bansil, A.; Felser, C.; Lin, H.; Hasan, M. Z. Discovery of Topological Weyl Fermion Lines and Drumhead Surface States in a Room Temperature Magnet. *Science* **2019**, *365*, 1278−1281.
(41) Shen, J. L.; Yao, Q. S.; Zeng, Q. Q.; Sun, H. Y.; Xi, X. K.; Wu, G. H.; Wang, W. H.; Shen, B. G.; Liu, Q. H.; Liu, E. K. Local Disorder-Induced Elevation of Intrinsic Anomalous Hall Conductance

Downloaded from pubs.acs.org/ancac3/article-pdf/20/30/21316/66049429/acsnano.6c06737.pdf by INST OF PHYSICS user on 30 September 2026

https://doi.org/10.1021/acsnano.6c06737
ACS Nano 2026, 20, 21316−21326

in an Electron-Doped Magnetic Weyl Semimetal. *Phys. Rev. Lett.* **2020**, *125*, No. 086602.
(42) Singha, R.; Roy, S.; Pariari, A.; Satpati, B.; Mandal, P. Planar Hall Effect in the Type-II Dirac Semimetal VAl_3. *Phys. Rev. B* **2018**, *98*, No. 081103(R).
(43) Wu, M.; Tu, D.; Nie, Y.; Miao, S.; Gao, W.; Han, Y.; Zhu, X.; Zhou, J.; Ning, W.; Tian, M. Novel $\pi/2$-Periodic Planar Hall Effect Due to Orbital Magnetic Moments in $MnBi_2Te_4$. *Nano Lett.* **2022**, *22*, 73−80.
(44) Nandy, S.; Sharma, G.; Taraphder, A.; Tewari, S. Chiral Anomaly as the Origin of the Planar Hall Effect in Weyl Semimetals. *Phys. Rev. Lett.* **2017**, *119*, No. 176804.
(45) Seemann, K. M.; Freimuth, F.; Zhang, H.; Blügel, S.; Mokrousov, Y.; Bürgler, D.; Schneider, C. Origin of the Planar Hall Effect in Nanocrystalline $Co_{60}Fe_{20}B_{20}$. *Phys. Rev. Lett.* **2011**, *107*, No. 086603.
(46) Wu, M.; Zheng, G. W.; Chu, Y.; Liu, Y.; Gao, W.; Zhang, H.; Lu, J.; Han, Y.; Zhou, J.; Ning, W.; Tian, M. Probing the Chiral Anomaly by Planar Hall Effect in Dirac Semimetal Cd_3As_2 Nanoplates. *Phys. Rev. B* **2018**, *98*, No. 161110.
(47) Kumar, N.; Guin, S. N.; Felser, C.; Shekhar, C. Planar Hall Effect in the Weyl Semimetal GdPtBi. *Phys. Rev. B* **2018**, *98*, No. 041103.
(48) Liu, Q. Q.; Fei, F. C.; Chen, B.; Bo, X. Y.; Wei, B. Y.; Zhang, S.; Zhang, M. H.; Xie, F. J.; Naveed, M.; Wan, X. G.; Song, F. Q.; Wang, B. G. Nontopological Origin of the Planar Hall Effect in the Type-II Dirac Semimetal $NiTe_2$. *Phys. Rev. B* **2019**, *99*, No. 155119.
(49) Xiao, X.; Li, J. X.; Ding, Z.; Wu, Y. Z. Four-Fold Symmetric Anisotropic Magnetoresistance of Single-Crystalline Ni (001) Film. *J. Appl. Phys.* **2015**, *118*, No. 203905.
(50) Ko, H.-W.; Park, H.-J.; Go, G.; Oh, J. H.; Kim, K.-W.; Lee, K.-J. Role of Orbital Hybridization in Anisotropic Magnetoresistance. *Phys. Rev. B* **2020**, *101*, No. 184413.
(51) Li, D. Z.; Pauly, F.; Smogunov, A. Giant Anisotropic Magnetoresistance through a Tilted Molecular π-Orbital. *Phys. Rev. Res.* **2020**, *2*, No. 033184.
(52) Park, S.; Woo, S.; Mele, E. J.; Min, H. K. Semiclassical Boltzmann Transport Theory for Multi-Weyl Semimetals. *Phys. Rev. B* **2017**, *95*, No. 161113(R).

Downloaded from pubs.acs.org/ancac3/article-pdf/20/30/21316/66049429/acsnano.6c06737.pdf by INST OF PHYSICS user on 30 September 2026

https://doi.org/10.1021/acsnano.6c06737
ACS Nano 2026, 20, 21316−21326